Room-temperature stabilization of commensurate 2D charge density waves and electronic twinning in TaS_2 using confined polytypes

Suk Hyun Sung,[1] Noah Schnitzer,[2,3] Steve Novakov,[4] Ismail El Baggari,[5] Xiangpeng Luo,[4] Jiseok Gim,[1] Nguyen Vu,[1] Todd Brintlinger,[6] Yuping Sun,[7] Kai Sun,[4] Liuyan Zhao,[4] Lena F. Kourkoutis,[8,3] John T. Heron,[1,9] and Robert Hovden[1,9]

[1]*Department of Materials Science and Engineering, University of Michigan, Ann Arbor, MI 48109*
[2]*Department of Materials Science and Engineering, Cornell University, Ithaca, NY 14853*
[3]*Kavli Institute at Cornell for Nanoscale Science, Ithaca, NY 14853*
[4]*Department of Physics, University of Michigan, Ann Arbor, MI 48109*
[5]*Department of Physics, Cornell University, Ithaca, NY 14853*
[6]*Materials Science and Technology Division, U.S. Naval Research Laboratory, Washington, D.C. 20375*
[7]*Key Laboratory of Materials Physics, Institute of Solid State Physics, Chinese Academy of Sciences, Hefei 230031, People's Republic of China*
[8]*School of Applied and Engineering Physics, Cornell University, Ithaca, NY 14853*
[9]*Applied Physics Program, University of Michigan, Ann Arbor, MI 48109*

(Dated: November 5, 2020)

Charge ordered transition metal dichalcogenides have distinct phenomena that govern exotic superconductivity and metal–insulator transitions, however, these quantum states only exist in two-dimensions (2D) or occur at low temperatures. Here we raise the critical temperature for spatially coherent charge density waves (e.g. C-CDW) in 1T-TaS_2 to well above room temperature by synthesizing interdigitated 2D polytypic heterostructures. The isolation of truly 2D CDWs between metallic layers reveals hidden electronic and structural ground states, including the emergence of a commensurate CDW at room-temperature and the restoration of mirror symmetries via interlayer CDW twinning. The twinned-commensurate CDW (tC-CDW) reported herein has a single metal–insulator phase transition at ∼350 K as measured structurally and electronically and the disordered nearly commensurate (NC)-CDW is no longer present. Advanced methods in scanned nanobeam diffraction and in-situ transmission electron microscopy identify and map the formation of twinned-commensurate charge density waves. This work introduces epitaxial polytype engineering of van der Waals materials to access 2D ground states distinct from conventional 2D fabrication.

Electronic control of collective electron states is a central goal of materials physics and the development of next-generation electronics and quantum materials [1–3]. TaS_2 and TaS_xSe_{2-x} host several charge density waves (CDW) that spontaneously break crystal symmetries, mediate metal–insulator transitions [4, 5], and compete with superconductivity [6, 7]. These quantum states are promising candidates for novel devices [8, 9], efficient ultrafast non-volatile switching [10], and suggest elusive chiral superconductivity [11]. Law & Lee recently called for pristine 2D CDW syntheses to access exotic spin-liquid states in 1T-TaS_2 [12]. Unfortunately, extrinsic disorder in free standing 2D layers degrades correlation-driven quantum behavior [13, 14] and clean-limit 2D charge density waves or superconductors are near absent [15]. Furthermore, like many materials, coherent quantum states occur at low temperature. Room temperature access to spatially coherent charge density waves (e.g. commensurate states) and clean-limit 2D confinement may enable a paradigm shift toward device logic and quantum computing.

Here we show the critical temperature for spatially coherent charge density waves (e.g. C-CDW) in 1T-TaS_2 can be raised to well above room temperature (∼150 K above the expected transition) by synthesizing clean interdigitated 2D polytypic heterostructures. This stabilizes a collective insulating ground state not expected to exist at room temperature. We show the formation of these spatially coherent states occurs when 2D CDWs are confined between metallic prismatic polytypes. Metallic layers screen impurity potentials to suppress the disordered NC-CDW phase. At the same time, interdigitation disables interlayer coupling between CDWs to ensure an unpaired electron in each 2D supercell. This raises the critical temperature of the C-CDW and forms out-of-plane twinned commensurate (tC) CDWs. Scanned nanobeam electron diffraction and high-resolution in-situ electron microscopy provide novel discovery of CDW structure across microns of area. These results demonstrate polytype engineering as a route to isolating 2D collective quantum states in a well-defined extrinsic environment with identical chemistry but distinct band structure.

Layered TaS_2 crystals are archetypal hosts to anomalous electronic properties associated with the formation of CDWs. The Ta coordination to six chalcogenides dramatically changes its behavior. Prismatic coordination (Pr) found in the 2H polytype is metallic, even below the CDW onset around 90 K, and becomes a superconductor around 0.5 K (enhanced to 2.2 K when thinned [16]). Octahedral (Oc) coordination found in the 1T polytype has inversion symmetry and exhibits three distinct CDW phases: commensurate (C), nearly-commensurate (NC), and incommensurate (IC). At room

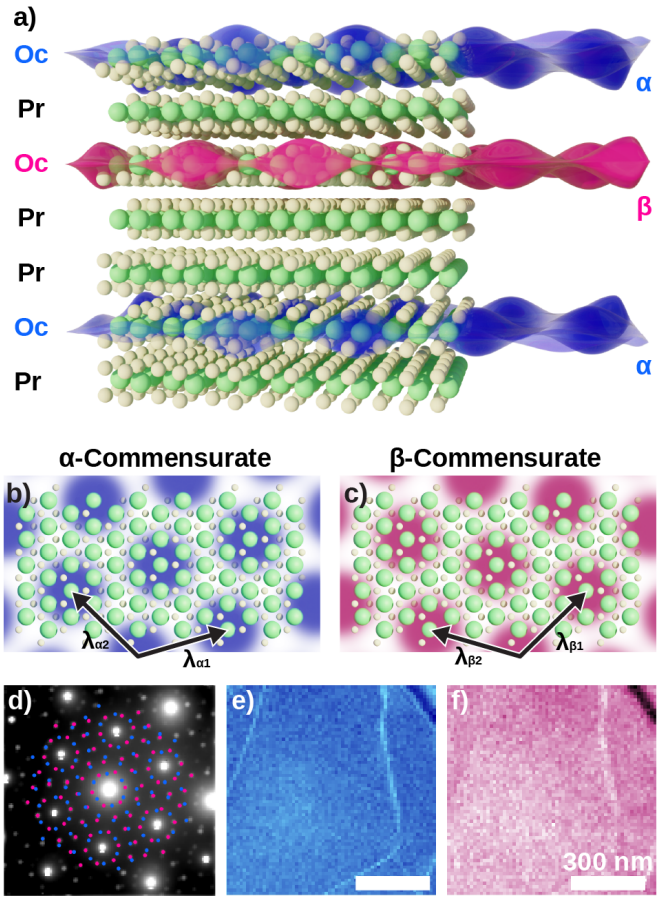

FIG. 1. **Twinned, commensurate CDW at room temperature in ultrathin TaS_2.** a) Schematic illustration of room-temperature, out-of-plane twinned, commensurate CDW in 1T-TaS_2. Blue and red overlays represent CDW twins within octahedrally coordinated TaS_2. Metallic prismatic polytypes isolate octahedral layers to stabilize tC-CDWs. b, c) Twin superlattice structure illustrated for α and β C-CDW, respectively. d) Average diffraction pattern of twinned, C-CDW state over $(870\ \text{nm})^2$ field-of-view reveals two sets of superlattice peaks (marked with blue and red). e, f) Nanobeam diffraction imaging from each set of superlattice peaks maps the coexistance of both CDW twins—expected for twinning out-of-plane.

temperature, the conductive NC-CDW is generally accepted as a C-CDW with short range order [17–19] that permits electron transport along regions of discommensuration [20, 21]. Below ∼200 K, the CDW wave vector locks into ∼13.9° away from the reciprocal lattice vector (Γ–M) to become a C-CDW that achieves long-range order with a $\sqrt{13} \times \sqrt{13}$ supercell [4, 22]. This reduction of crystal symmetry gaps the Fermi-surface and the commensurate phase becomes Mott insulating [4, 23, 24]. At these low temperatures, CDWs in TaS_2 have been manipulated under voltage bias [14, 25]. Above 352 K, the CDW wave vector aligns along the reciprocal lattice vector and becomes the disordered IC-CDW phase.

The tC-CDW phase reported herein has distinct out-of-plane charge order—illustrated in Figure 1a. 2D CDWs reside within Oc-layers sparsely interdigitated between metallic Pr-layers. Each CDW is commensurate in one of two degenerate twin states, α-C (blue) or β-C (red) (Figure 1b, c). The translational symmetry is described by in-plane CDW lattice vectors $\boldsymbol{\lambda}_\alpha = 3\mathbf{a}_1 - \mathbf{a}_2$ and $\boldsymbol{\lambda}_\beta = 4\mathbf{a}_1 + \mathbf{a}_2$.

CDWs are a prototypical manifestation of electron-lattice coupling, in which both the electron density and lattice positions undergo periodic modulations to reduce crystal symmetry and lower the electronic energy [26]. The associated periodic lattice distortions (PLD) diffract incident swift electrons into low-intensity superlattice peaks between Bragg peaks [27, 28] (See also: Supplemental section SI1). Figure 1d shows the position averaged convergent beam electron diffraction pattern (0.55 mrad semi-convergence angle, 80 keV) of the tC-CDW phase at room temperature with α, β superlattice peaks annotated (blue, red). Regularly spaced superlattice peaks and bright first order superlattice peaks are characteristic of C-CDWs and match the tC-CDW peaks.

Both α and β CDW states were mapped over microns of area to reveal a uniform co-existence of both twins when viewed in projection out-of-plane (Fig. 1e,f). This is evidently different from recently reported in-plane twin CDWs created by femtosecond light pulses [29]. CDW structure was imaged using the diffracted intensity of every α or β superlattice peak from a convergent electron beam (Fig. 1e, f) rastered across the specimen—an emerging technique often called 4D-STEM (See Methods) [30–32]. In this way, the local CDW structure was measured at ∼4.6 nm resolution and across >1 μm fields of view. Previous approaches to mapping CDWs entailed sparse measurement from a handful diffraction patterns [29], tracking every atomic displacement [33], or traditional dark-field TEM techniques utilizing a single diffraction peak that result in low resolution and debilitating signal-to-noise ratios [4, 34].

Thermal treatment reproducibly forms the tC-CDW phase—a process summarized by the in-situ selected area electron diffraction (SAED) in Figure 2a. Initially, an exfoliated flake of 1T-TaS_2 hosts NC-CDWs (Fig. 2a, left) at room temperature with diffuse first-order superlattice peaks (cyan circles) and sharp second order superlattice peaks (cyan triangle). 1T-TaS_2 is heated past the reversible phase transition ($T_{\text{NC-IC}} \approx 352$ K) into the disordered IC-CDW state, which has characteristic azimuthally diffuse superlattice spots (Fig. 2a, right). Heating continues up to temperatures (∼720 K) above the polytype transition ($T_{\text{Oc-Pr}} \approx 600$ K [35]) where it remains for several minutes (see Methods). Upon cooling, the system does not return to the expected NC-CDW but instead enters a tC-CDW state with sharp, commensurate first and second order superlattice peaks duplicated with mirror symmetry (α, β) (Fig. 2a, bottom). The tC-CDW phase is stable and observable after months of dry storage (RH ∼10 %) at room temperature. Synthesis was replicated ex-situ in both high-vacuum ($< 10^{-7}$

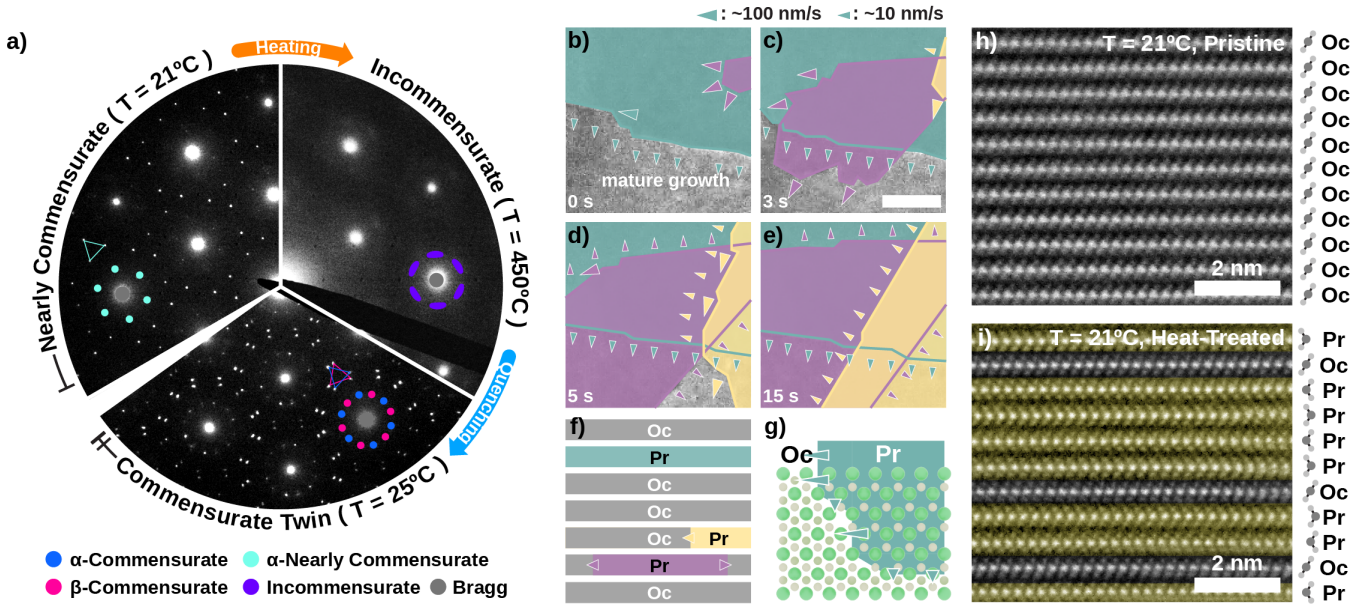

FIG. 2. **Polytype isolation forms 2D CDW layers.** a) Pristine 1T-TaS_2 shows a reversible NC (left)⇋IC (right) transition at ∼352 K. Upon thermal treatment, the NC phase disappears, and stable room temperature state becomes tC-CDW (bottom). b–e) In-situ TEM reveals layer-by-layer octahedral to prismatic polytypic transformations during heat treatment. Multiple polytypic domains (denoted green, purple, and yellow) nucleate and grow simultaneously without interaction (See Supplemental Video). Scale bar is 350 nm. f) Schematic cross-section of TaS_2 during layer-by-layer polytypic transition. g) Fast and slow transitions occur along $\langle 10\bar{1}0\rangle$ and $\langle 11\bar{2}0\rangle$ directions respectively. h–i) Atomic resolution cross-sectional HAADF-STEM of h) pristine and i) heat-treated TaS_xSe_{2-x} confirms polytypic transformation. After treatment, prismatic (Pr) layers encapsulate monolayers of octahedral (Oc) layers. A selenium doped sample was imaged to enhance chalcogen visibility.

Torr) and inert argon purged gloveboxes, but amorphized in ambient air. The tC-CDW was equivalently synthesized for both TaS_2 and TaS_xSe_{2-x}.

Heating above the polytype transition temperature ($T_{Oc\text{-}Pr}$) provokes layer-by-layer transitions from Oc to Pr polytypes instead of a rapid bulk transformation. Figure 2b–e shows in-situ TEM using high-frame-rate (25 fps) microscopy taken at ∼710 K. Each colored overlay highlights the growth and formation of a new prismatic polytype domain (raw data in Supp. Fig. S2). Arrows indicate movement of Oc/Pr coordination boundary with a fast-transition up to $\sim 10^2$ nm/s along $\langle 10\bar{1}0\rangle$ crystal directions and a slow-transition at ∼10 nm/s along $\langle 11\bar{2}0\rangle$ (Fig. 2g). Video of the transformation is striking (Supplemental Video). Domains nucleate and boundaries progress independently between layers as illustrated in Figure 2b-f. Cooling the sample mid-transition produces a sparsely interdigitated polytypic heterostructure.

Atomic resolution cross-section images of pristine and heat-treated samples (Fig. 2h and i, respectively) measured by high-angle annular dark-field (HAADF)-STEM reveal the interdigitated polytypic heterostructure. Interdigitation creates monolayers of octahedral (Oc) coordination that host 2D CDWs in a clean, defect-free environment of prismatic (Pr) metallic layers.

The metallic 'Pr' layers are hypothesized to screen out-of-plane interactions and impurity potentials to stabilize low-temperature commensurate CDWs at room temperature. As a result, the NC-CDW state no longer exists and a long-range ordered tC-CDW emerges as a stable phase up to ∼350 K. This result is radically different from previous reports where free standing ultra-thin 1T-TaS_2 degrades long-range order [36] and broadens the NC-CDW phase by lowering T_{CCDW} [14, 25, 37]. However, our observation of 2D commensurate CDWs agrees with a theoretical prediction that commensurate CDWs are more stable in clean monolayer [38]. Understanding the role of disorder requires decoupling intrinsic quantum behavior from extrinsic influences at the surfaces, especially in low dimensions where long-range order becomes more fragile and vulnerable to impurities [13, 39, 40]. When the disorder strength reaches a certain threshold, the long-range commensurate CDW phase gives its way to a disordered phase [13]. Here, each 2D 1T-TaS_2 CDW is in its native chemical, epitaxial, and unstrained environment. Impurity potentials that pin CDWs [41] and break spatial coherence are mitigated by adjacent metallic Pr-layers. For commensurate CDWs (in 2D and above) in the presence of sufficiently weak disorder, the charge order remains stable [40]. Additionally, isolating monolayers of 1T-TaS_2 ensures an odd number of electrons per unit cell and elongates the Fermi surface along c-axis—both expected to reduce the electronic energy.

In tC-CDW, metallic Pr-layers decouple interlayer CDW interactions to create isolated 2D CDWs with twin degeneracy. Using a phenomenological Landau model we

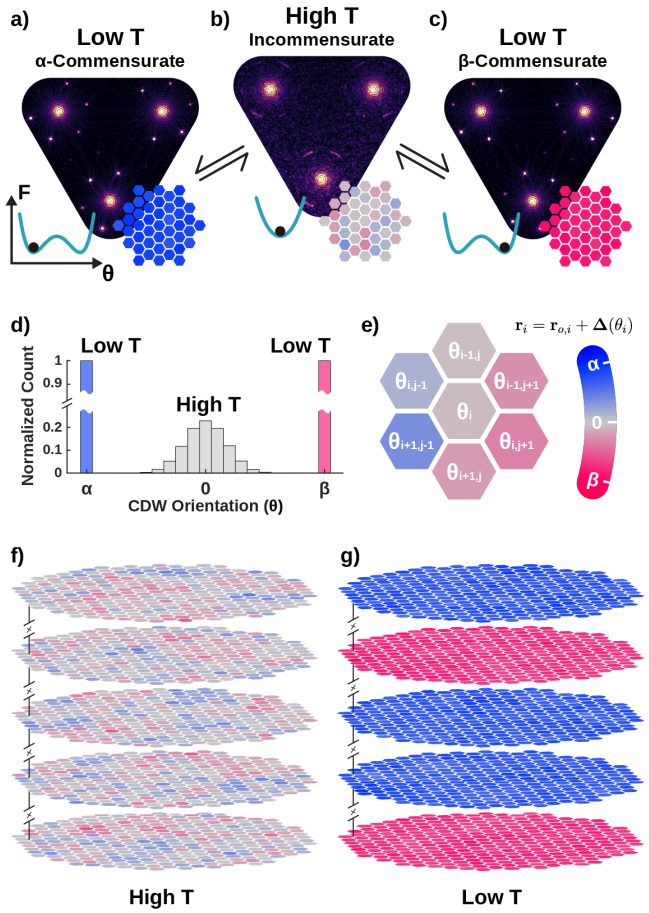

FIG. 3. **Phenomenological Landau model illustrates formation of commensurate CDWs with out-of-plane twin degeneracy.** a–c) The CDW wave-vector direction θ defines an order parameter with degenerate commensurate twins when cooled from IC-CDW phase. Simulated far-field diffraction patterns for a) α-C, b) IC and c) β-C. The free energy (F) landscape (Inset-left) governs the mean θ and the real-space distribution (Inset-right). d) Histogram of θ shows zero-centered, wide distribution at high temperature. At low temperature, the distribution is narrow and centered at $\pm 13.9°$ for either twin. e) Six nearest-neighbor interactions drives long-range order of the CDW. f) At high temperature θ is mean centered and disordered, however, g) at low-temperature each 2D layer converges into either α or β randomly when layers are decoupled.

illustrate a kinetic pathway for accessing the tC-CDW. Here, local orientation of the CDW wave vector, θ, is an apt order parameter for describing symmetry breaking of C⇋IC transitions (See Methods). A Landau free energy expansion of this order parameter combined with an XY interaction of the CDW wave vector (see Methods) qualitatively reproduces diffraction patterns for IC-CDW and α/β C-CDW. In diffraction, the superlattice peak location and shape encodes the distribution of the CDW order parameter. Simulated diffraction patterns at high temperatures feature first-order superlattice peaks azimuthally broadened by CDW disorder and centered along the reciprocal lattice (Γ–M) direction (Fig. 3b). At low temperature, the superlattice peaks are sharpened by long-range CDW order and located at $+13.9°$ or $-13.9°$ away from Γ–M (Fig. 3a,c). Figure 3d shows distribution of θ at high (gray) and low (blue, red) temperatures.

When cooled, the system chooses α or β with equal probability. For pristine 1T-TaS_2, CDWs couple between layers, twin degeneracy is broken, and no twinning occurs [42]. However, in the absence of interlayer interaction or extrinsic perturbation, each 2D CDW layer quenches randomly into either α or β C-CDW (Fig. 3g) from the high-temperature IC-CDW phase (Fig. 3f)—forming the out-of-plane twinned tC-CDW phase. From our model, out-of-plane twinning occurs for modest cooling rates but we note fast quenching predicts in-plane twinning (Supplemental figure S5) similar to reported ultrafast optical excitations [29] .

Rotational-anisotropy second-harmonic generation (RA-SHG) revealed restoration of twin degeneracy in heat-treated samples. The RA-SHG of pristine sample (Fig. 4b) exhibits a hallmark of the RA-SHG pattern rotated ∼20.9° away from the lattice vectors; breaking mirror symmetry due to formation of a single-domain NC-CDW. In contrast, the heat-treated sample's RA-SHG pattern (Fig. 4c) is mirror-symmetric to the crystalline directions and much stronger SHG signal. These are strong evidences of equally weighted degenerate α and β states (i.e., tC-CDW) and the emergence of Pr-layers that are mirror symmetric and non-centrosymmetric.

Electronic measurement of the polytypic heterostructure with interdigitated CDWs reveals a direct tC⇋IC transition at 350 K and removal of disordered NC-CDW phase. Figure 4a shows in-plane resistance vs. temperature measurements of pristine 1T (pink) and heat-treated polytypic heterostructure (blue) are drastically different. The heterostructure features only one metal–insulator transition at 350 K, whereas pristine 1T-TaS_2 exhibits two transitions at ∼200 K (C⇋NC) and 350 K (NC⇋IC). Resistance jumps are a signature of emergent CDW order. At low temperature the metallic Pr layers dominate in-plane conduction since the resistance is expected to monotonically decrease as observed in bulk material [43]. This hinders the quantification of resistance in individual Oc-layers, however the critical temperatures remain clearly visible.

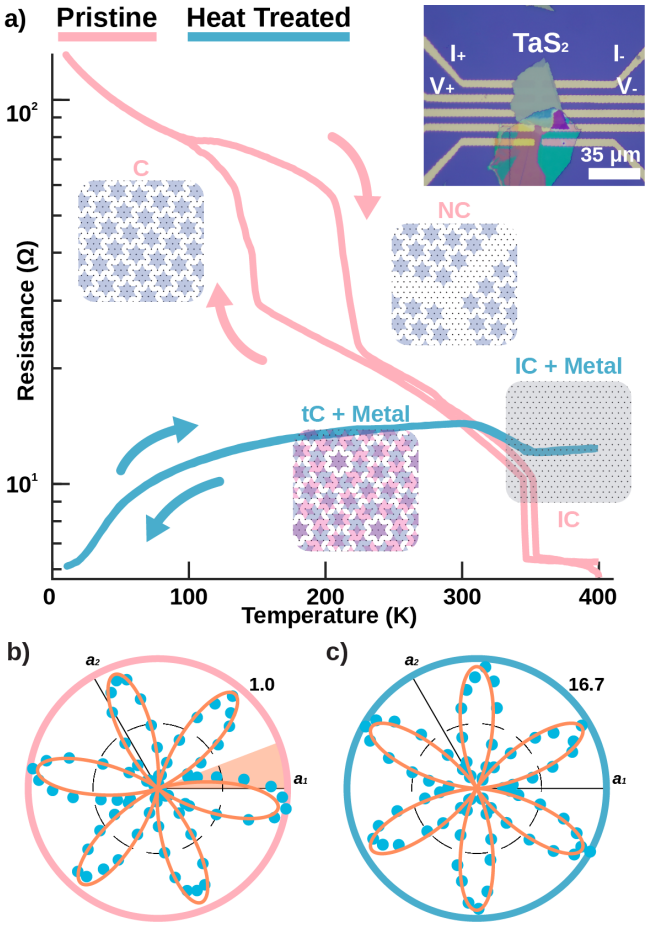

FIG. 4. **Electronic transport of tC-CDW phase transition and reversibility.** a) 4-point in-plane resistance measurement as function of temperature for pristine bulk (pink) and heat-treated (blue) TaS_2. Pristine samples show two jumps in resistance for C⇋NC and NC⇋IC, whereas the heat treated polytypic heterostructures only feature a single, reversible tC⇋IC transition at ∼350 K corresponding to the enhanced critical temperature for CDW commensuration and dissapearance of the NC-CDW. Metallic Pr-layers dominate the overall trend of the resistance measurement, however, the single jump above room-temperature is a distinct feature of the tC-CDW. Inset) Optical image of the nanofabricated device. b) The RA-SHG pattern for pristine 1T samples display a mismatch between the nominal mirror direction and the crystalline direction, indicating the CDW breaks mirror symmetry. c) After heat treatment, the RA-SHG pattern is symmetric with respect to the crystal, implying equal weights between the α and β states. The SHG intensity also increases with mirror symmetric Pr-layers present

Repeated in-situ heating–cooling cycles reveal the tC⇋IC transition is reversible and the NC-CDW phase is removed. Electronic measurements (Fig. 4a) match structure measurements from in-situ SAED (Fig. 2a) and confirm the insulating commensurate charge order of the tC-CDW phase. The interdigitated polytype herein stabilizes coherent electronic states well above (∼150 K) the normal critical temperature, and disordered NC-CDW phase is structurally and electronically removed.

In summary, the long-range ordered CDW state was stabilized at room-temperature by reducing its dimension to 2D using engineered interdigitated polytypes of TaS_2. The metallic layers isolate each 2D CDW to restore twin degeneracy giving rise to an out-of-plane twinned commensuratate CDW phase. 4D-STEM mapped twinned CDW order across large fields-of-view (∼1 μm) to confirm twin structure and atomic resolution HAADF-STEM revealed the 2D Oc-layers embedded in metallic Pr-layers. Both structural and electronic investigations show that the disordered NC-CDW phase disappears for a 2D CDW in a chemically and epitaxially native environment. The stabilization of the tC-CDW phase illustrates 2D polytype engineering as a new route to exotic correlated electron states.

ACKNOWLEDGMENTS

R.H. and S.H.S. acknowledge the financial support of the W.M. Keck Foundation. L. Z. acknowledges support by the NSF CAREER Grant No. DMR-1749774. Experiments were conducted using the Michigan Center for Materials Characterization (MC2) with assistance from Haiping Sun and Bobby Kerns and the NSF-PARADIM platform (No. DMR-1539918) at Cornell University. This work was performed in part at the University of Michigan Lurie Nanofabrication Facility with assistance from Pilar Herrera-Fierro, Vishva Ray, and Sandrine Martin—supported by the National Science Foundation Major Research Instrumentation award under No. DMR-1428226. We thank Lu Li helpful for discussion.

S.H.S., N.S. and R.H. performed HAADF-STEM and in-situ TEM. S.H.S., N.S., R.H., I.E.B. and L.F.K. performed 4D-STEM experiments. S.H.S., S.N., J.G, T.B. and J.T.H. fabricated samples for electronic measurements. S.N., N.V. and J.T.H. performed electronic measurements. X.L. and L.Z. performed RA-SHG measurements. Y.S. grew 1T-TaS_xSe_{2-x} crystals. S.H.S., R.H. and K.S. provided theoretical interpretation. S.H.S. and R.H. prepared the manuscript. All authors reviewed and edited the manuscript.

[1] D. N. Basov, R. D. Averitt, and D. Hsieh, Nat. Mater. **16**, 1077 (2017).
[2] B. Keimer and J. E. Moore, Nat. Phys. **13**, 1045 (2017).
[3] Y. Tokura, M. Kawasaki, and N. Nagaosa, Nat. Phys **13**, 1056 (2017).
[4] J. Wilson, F. Di Salvo, and S. Mahajan, Adv. Phys. **24**,

117 (1975).
[5] F. Boswell and A. Prodan, Mater. Res. Bull. **19**, 93 (1984).
[6] E. Navarro-Moratalla, J. O. Island, S. Mañas-Valero, E. Pinilla-Cienfuegos, A. Castellanos-Gomez, J. Quereda, G. Rubio-Bollinger, L. Chirolli, J. A. Silva-Guillén, N. Agraït, G. A. Steele, F. Guinea, H. S. J. van der Zant, and E. Coronado, Nat. Commun. **7**, 11043 (2016).
[7] R. F. Frindt, Phys. Rev. Lett. **28**, 299 (1972).
[8] M. J. Hollander, Y. Liu, W.-J. Lu, L.-J. Li, Y.-P. Sun, J. A. Robinson, and S. Datta, Nano Lett. **15**, 1861 (2015).
[9] G. Liu, B. Debnath, T. R. Pope, T. T. Salguero, R. K. Lake, and A. A. Balandin, Nat. Nanotechnol. **11**, 845 (2016).
[10] I. Vaskivskyi, I. A. Mihailovic, S. Brazovskii, J. Gospodaric, T. Mertelj, D. Svetin, P. Sutar, and D. Mihailovic, Nat. Commun. **7**, 11442 (2016).
[11] A. Ribak, M. R. Skiff, M. Mograbi, P. K. Rout, M. H. Fishcer, J. Ruhman, K. Chashka, Y. Dagan, and A. Kanigel, Sci. Adv. **6**, eaax9480 (2020).
[12] K. Law and P. Lee, Proc. Natl. Acad. Sci. **114**, 6996 (2017).
[13] L. Nie, G. Tarjus, and S. A. Kivelson, Proceedings of the National Academy of Sciences **111**, 10.1073/pnas.1406019111 (2014).
[14] Y. Yu, F. Yang, X. F. Lu, Y. J. Yan, Y.-H. Cho, L. Ma, X. Niu, S. Kim, Y.-W. Son, D. Feng, S. Li, S.-W. Cheong, X. H. Chen, and Y. Zheng, Nat. Nanotechnol. **10**, 270 (2015).
[15] A. Devarakonda, H. Inoue, S. Fang, C. Ozsoy-Kesinbora, M. Kriener, L. Fu, E. Kaxiras, D. Bell, and J. Checkelsky, Science , 231 (2020).
[16] E. Navarro-Moratalla, J. Island, S. Mañas-Valero, E. Pinella-Cienfuegos, A. Castellanos-Gomez, J. Quereda, G. Rubio-Bollinger, L. Chirolli, J. A. Silva-Guillen, N. Agrait, G. A. Steele, F. Guinea, H. S. J. van der Zand, and E. Coronado, Nat. Commun. **7**, 11043 (2016).
[17] X. L. Wu and C. M. Lieber, Science **243**, 1703 (1989).
[18] S. Vogelgesang, G. Storeck, J. G. Horstmann, T. Diekmann, M. Sivis, S. Schramm, K. Rossnagel, S. Schäfer, and C. Ropers1, Nat. Phys. **14**, 184 (2017).
[19] R. Hovden, A. W. Tsen, P. Liu, B. H. Savitzky, I. El Baggari, Y. Liu, W. Lu, Y. Sun, P. Kim, A. N. Pasupathy, and L. F. Kourkoutis, Proc. Natl. Acad. Sci. **113**, 11420 (2016).
[20] D. Cho, S. Cheon, K.-S. Kim, S.-h. Lee, Y.-H. Cho, S.-W. Cheong, and H. W. Yom, Nat. Commun. **7**, 10453 (2016).
[21] B. Sipos, A. F. Kusmartseva, A. Akrap, H. Berger, L. Forro, and E. Tutis, Nat. Mater. **7**, 960 (2008).
[22] T. Ishiguro and H. Sato, Phys. Rev. B **44**, 2046 (1991).
[23] M. D. Johannes and I. I. Mazin, Phys. Rev. B **77**, 165135 (2008).
[24] K. Rossnagel, J. Phys.: Condens. Matter **23**, 213001 (2011).
[25] A. W. Tsen, R. Hovden, D. Wang, Y. D. Kim, J. Okamoto, K. A. Spoth, Y. Liu, W. Lu, Y. Sun, J. C. Hone, L. F. Kourkoutis, P. Kim, and A. N. Pasupathy, Proc. Natl. Acad. Sci. **112**, 15054 (2015).
[26] W. L. McMillan, Phys. Rev. B **12**, 1187 (1975).
[27] A. W. Overhauser, Phys. Rev. B **3**, 3173 (1971).
[28] I. El Baggari, B. H. Savitzky, A. S. Admasu, J. Kim, S.-W. Cheong, R. Hovden, and L. F. Kourkoutis, Proc. Natl. Acad. Sci. **115**, 1445 (2018).
[29] A. Zong, X. Shen, A. Kogar, L. Ye, C. Marks, D. Chowdhury, T. Rohwer, B. Freelon, S. Weathersby, R. Li, J. Yang, J. Checkelsky, X. Wang, and N. Gedik, Sci. Adv. **4** (2018).
[30] M. W. Tate, P. Purohit, D. Chamberlain, K. X. Nguyen, R. Hovden, C. S. Chang, P. Deb, E. Turgut, J. T. Heron, D. G. Schlom, and et al., Microsc. Microanal. **22**, 237–249 (2016).
[31] O. Panova, C. Ophus, C. J. Takacs, K. C. Bustillo, L. Balhorn, A. Salleo, N. Balsara, and A. M. Minor, Nat. Mater. **18**, 860 (2019).
[32] Q. Qiao, S. Zhou, J. Tao, J. Zheng, L. Wu, S. T. Ciocys, I. Maria, D. J. Srolovitz, G. Karapetrov, and Y. Zhu, Phys. Rev. Mat. **1**, 054002 (2017).
[33] B. H. Savitzky, I. El Baggari, A. S. Admasu, J. Kim, S.-W. Cheong, R. Hovden, and L. F. Kourkoutis, Nat. Commun. **8**, 1883 (2017).
[34] C. H. Chen, J. M. Gibson, and R. M. Fleming, Phys. Rev. B **26**, 184 (1982).
[35] F. L. Givens and G. E. Fredericks, J. Phys. Chem. Solids **38**, 1363 (1977).
[36] D. Sakabe, Z. Liu, K. Suenaga, K. Nakatsugawa, and S. Tanda, npj Quantum Mater. **2**, 22 (2017).
[37] M. Yoshida, Y. Zhang, J. Ye, R. Suzuki, Y. Imai, S. Kimura, A. Fujiwara, and Y. Iwasa, Sci. Rep. **4**, 7302 (2014).
[38] P. Darancet, A. J. Millis, and C. A. Marianetti, Phys. Rev. B **90**, 045134 (2014).
[39] Y. Imry and S.-k. Ma, Physical Review Letters **35**, 1399 (1975).
[40] J. Cardy, *Scaling and renormalization in statistical physics*, Vol. 5 (Cambridge university press, 1996).
[41] T. M. Rice, S. Whitehouse, and Littlewood, Phys. Rev. B. **24**, 2751–2759 (1981).
[42] W. L. McMillan, Phys. Rev. B **14**, 1496 (1976).
[43] A. H. Thompson, F. R. Gamble, and R. F. Koehler, Phys. Rev. B **5**, 2811 (1972).

Appendix A: Methods

1. Electron Microscopy

Mapping CDW structure required a pixel array detector to collect a convergent beam electron diffraction pattern at every beam position across large fields-of-view (i.e. 4D-STEM). In-situ 4D-STEM was performed on FEI Titan Themis 300 (80 keV, 0.55 mrad convergence semi-angle) with electron microscope pixel array detector (EMPAD) and DENS Wildfire heating holder. For 4D-STEM, a convergent beam electron diffraction (CBED) pattern was recorded at each beam position using the EMPAD detector. EMPAD's high dynamic range (1,000,000:1) and single electron sensitivity [30] allows simultaneous recording of intense Bragg beams alongside weak superlattice reflections. Virtual satellite dark field images were formed by integrating intensities from all satellite peaks at each scan position.

In-situ TEM revealed layer-by-layer polytypic transi-

tion. The polytype difference is indiscernible in low-magnification with HAADF-STEM, as two polytypes have equal density. However, the change in bond coordination at polytype boundaries provide visible coherent contrast in TEM. The in-situ movie and SAED patterns were taken with JEOL 2010F (operated at 200 keV) with Gatan Heater Holder and Gatan OneView Camera. Both sample for 4D-STEM and TEM were prepared by exfoliating bulk 1T-TaS_2 crystal on to PDMS gel stamp, then transferring on to a TEM grid.

Cross-sectional HAADF-STEM images were taken on JEOL 3100R05 (300 keV, 22 mrad) with samples prepared on FEI Nova Nanolab DualBeam FIB/SEM.

2. Thermal Synthesis of tC-CDW in TaS_2

Interdigitated 2D TaS_2 polytypes were synthesized by heating 1T-TaS_2 to 720 K in high vacuum ($< 10^{-7}$ Torr) or in an argon purged glovebox. 1T-TaS_2 was held at 720 K for ∼10 minutes, then brought down to room temperature. Once the interdigitated polytype is fully established, tC-CDW becomes stable electronic state up to 350 K. Synthesis is sensitive the duration held at high temperature. Notably, if the sample is not held long enough at elevated temperature, NC-C twin phase was reached (See Supplemental Figure S6), due to sparse distribution of Pr-layers encapsulating multilayer 1T-TaS_2. Both slow (∼1 K/sec) and fast (∼10 K/sec) cooling rate produced out-of-plane twinning.

3. Device Fabrication and Electronic Measurement

Sample lithography was done with a standard SPR-220 based process using a Heidelberg μPG 501 maskless exposure tool to directly expose samples. The bottom contact pattern was exposed on a silicon wafer with 500 nm SiO_2. To limit damage and bending to the TaS_2 flakes, the bottom contact liftoff pattern was first ion beam etched with Ar to a 60 nm depth. The trenches were then back-filled with 10 nm Ti and 50 nm Au, deposited in an e-beam evaporator at 3 Å/s, and excess metal was lifted-off using acetone/isopropanol sonication of the wafer. The resulting contacts are level to the wafer surface to within 5 nm, as confirmed by AFM. Before flake exfoliation, the bottom contacts were gently polished using 100 nm micropolishing film to remove liftoff fingers, which can extend up to 30 nm above the wafer surface. Each bottom contact pattern includes six 5 μm striplines spaced 5 μm apart, and eight radial pads of approximately 500×500 μm for top contact fan-out.

Resistance vs. temperature measurements were performed in a Quantum Design Dynacool PPMS using a standard sample puck and an external Keithley 2400 series source meter. The sample was adhered to the puck backplane with silver paint, and contacts were wire bonded to the puck channel pads using 50 μm Au wire. To ensure sample thermalization, a baffle rod with an Au-coated sealing disk hovering <1 cm above the sample was inserted into the PPMS bore, and the heating and cooling rate was restricted to <2 K/min. Depending on sample characteristics, between 20–200 μA current was sourced for four wire measurements. The current/voltage limits were chosen to keep electric fields below 10 kV/cm to avoid sample breakdown, as well as to keep current densities below 10^5A/cm^2 and prevent localized heating at low temperatures. Due to sample variability, such as inter-layer CDW phase differences and mechanical variability such as tears or holes in flakes, these limits are approximate in general scanning. In cases where samples transformed into bulk prismatic phase, they are better observed.

4. Modelling C⇌IC transition

We describe the free energy landscape using Landau expansion:

$$f_i(T) = a_2(T - T_c)\theta_i^2 + \mathrm{a}_4\theta_i^4 + \sum_{nn}^{6} \cos(\theta_{nn} - \theta_i)^2 \quad \text{(A1)}$$

with f, T, T_c, a, θ denotes local free energy, temperature, transition temperature, Landau energy coefficient, and local CDW orientation respectively. The last term is an XY nearest-neighbor interaction that enforces smoothness; in the continuum limit, it converges to $|\nabla\theta|^2$. We chose 6 nearest-neighbors to accommodate the crystal symmetry (Fig. 3c). The simulation was done on hexagonal grid with 65536 sites and periodic boundary condition.

The distribution of θ was calculated using Markov Chain Monte Carlo simulation with Metropolis-Hasting algorithm. Initially, a random distribution θ was generated. At each iteration, 40% of sites were randomly selected, then randomly generated θ were accepted or rejected based on Boltzmann statistics: $\exp[-\Delta f/k_BT]$. The effect of cooling was simulated in simulated annealing manner where initial T was set to 2 T_c then reduced by 0.2 T_c every 10^{10} iterations.

To simulate far-field diffraction from simulated θ, each lattice position ($\mathbf{r}_i$) was distorted with three longitudinal modulation waves with wave vector $\mathbf{q}_{i,1}, \mathbf{q}_{i,2}, \mathbf{q}_{i,3}$ along θ_i, θ_i+120°, θ_i+240°: $\mathbf{r}'_i = \mathbf{r}_i + \sum_{n=1,2,3} \mathbf{A}_n \sin(\mathbf{q}_{i,n} \cdot \mathbf{r}_i)$. Far-field diffraction ($I(\mathbf{k})$) was calculated by taking modulus squared of plane waves from each lattice sites: $I(\mathbf{k}) = |\sum_i \exp[i\mathbf{k} \cdot \mathbf{r}'_i]|^2$.

5. RA-SHG Measurements

The RA-SHG measurements were performed with the beam at normal incidence. The reflected SHG intensity is recorded as a function of the azimuthal angle between the incident electric polarization and the in-plane crystalline

a-axis, with the reflected electric polarization being parallel to the incident one. In this experiment, the incident ultrafast light source was of 800 nm wavelength, 50 fs pulse duration and 200 kHz repetition rate, and was focused with a 5 μm diameter spot on the sample with a fluence of $\sim$0.2 mJ/cm^2. The intensity of the reflected SHG was measured with a single photon counting detector. SHG measurements was performed on TaS_xSe_{2-x} sample, which has same point group symmetries with TaS_2 both before and after heat treatment.

Supplementary Materials: Room temperature stabilization of commensurate charge density waves and electronic twinning in ultrathin TaS_2

Suk Hyun Sung, et al.

Appendix SI1: Periodic Lattice Displacements (PLDs) in Charge Density Wave (CDW) Materials

CDWs are accompanied by PLDs that displace nuclei positions and manifest as an array of superlattice satellite peaks in diffraction patterns. The reciprocal superlattice structure was first described for single PLD by Overhauser [27] and for any number of harmonics by Hovden et alia [19]. In PLD model, nuclei position ($\mathbf{r}'_i$) from their original positions ($\mathbf{r}_i$) with sinusoidal displacement fields and their n^{th} order harmonics: $\mathbf{r}'_i = \mathbf{r}_i + \sum_n \mathbf{A}_n \sin(\mathbf{q}_n \cdot \mathbf{r} + \phi_n)$. $\mathbf{A}$, $\mathbf{q}$, ϕ denotes displacement vector, wave vector and phase of the modulation wave. Resulted diffraction pattern $\mathrm{I}(\mathbf{k})$ is proportional to squared modulus of the planes waves from each atom:

$$\begin{aligned} \mathrm{I}(\mathbf{k}) &\propto \left| \sum_i \exp[(i\mathbf{k} \cdot \mathbf{r}'_i)] \right|^2 \\ &= \left| \sum_{i,j} \sum_{\alpha_n} \delta(\mathbf{k} - \mathbf{b}_{i,j} - \sum_n \alpha_n \mathbf{q}_n) \times \prod_n \exp[(i\alpha_n \phi_n) J_{\alpha_n}(\mathbf{k} \cdot \mathbf{A}_n)] \right|^2, \end{aligned} \tag{SI1}$$

where $\mathbf{b}_{i,j}$ is reciprocal lattice vector and J denotes Bessel function of first kind.

The δ-function term maps out Bragg peaks (at $\mathbf{b}_{i,j}$) and satellite peaks ($\alpha_n \mathbf{q}_n$) away from Bragg peaks. The second term determines intensity of each diffraction peak. Transversity (i.e. angle between $\mathbf{q}$ and $\mathbf{A}$) contributes significantly to the structure of diffraction pattern through $\mathbf{k} \cdot \mathbf{A}$ term.

Appendix SI2: In-situ TEM SAED Patterns

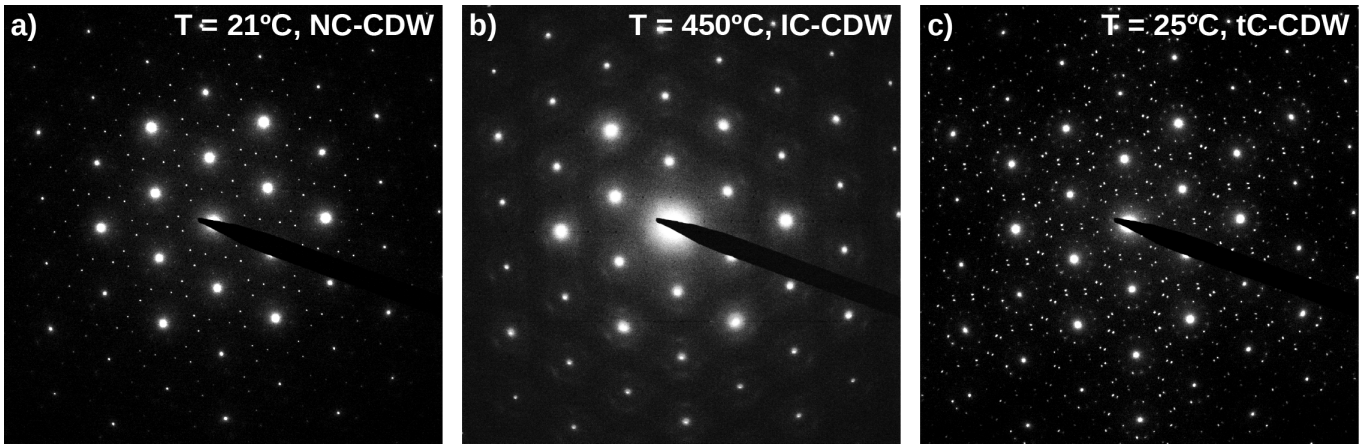

SFIG. S1. **In-situ SAED of NC-CDW to tC-CDW evolution.** a) NC-CDW phase 1T-TaS_2 SAED pattern features characteristic bright second order and diffused 1st order superlattice reflections. b) At above 350 K, IC-CDW emerges where superlattice peaks are diffused azimuthaly and second order peaks vanishes. c) Heating above 720 K produces interdigitated polytypic heterostructure, which hosts a long-range ordered, coherent tC-CDW phase at room temperature

Appendix SI3: In-situ TEM of TaS_2 polytype transformation

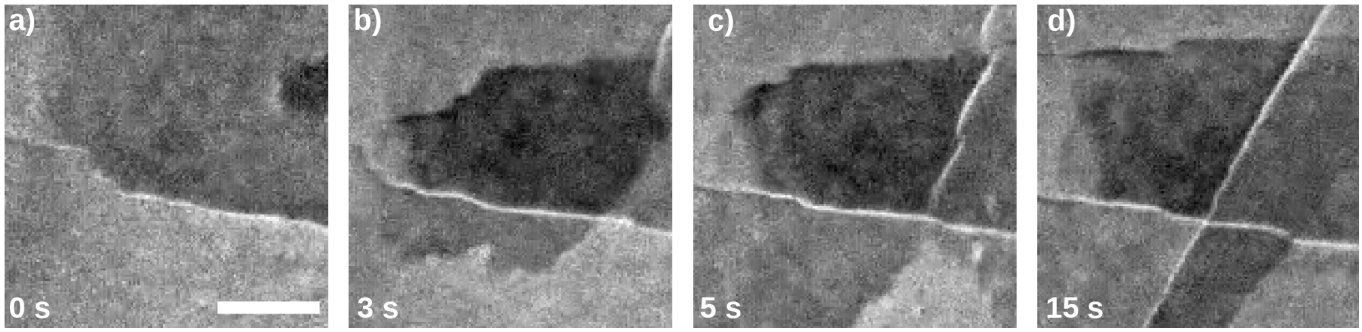

SFIG. S2. **In-situ TEM images of layer-by-layer Octahedral to Prismatic polytypic transition** In-situ TEM still frames reveal Oc to Pr interpolytypic transition. Domain boundaries propagate without interacting with each other—telltale sign of layer-by-layer transition. The high framerate recording is provided as a Supplemental Video.

Appendix SI4: Cross-sectional HAADF-STEM

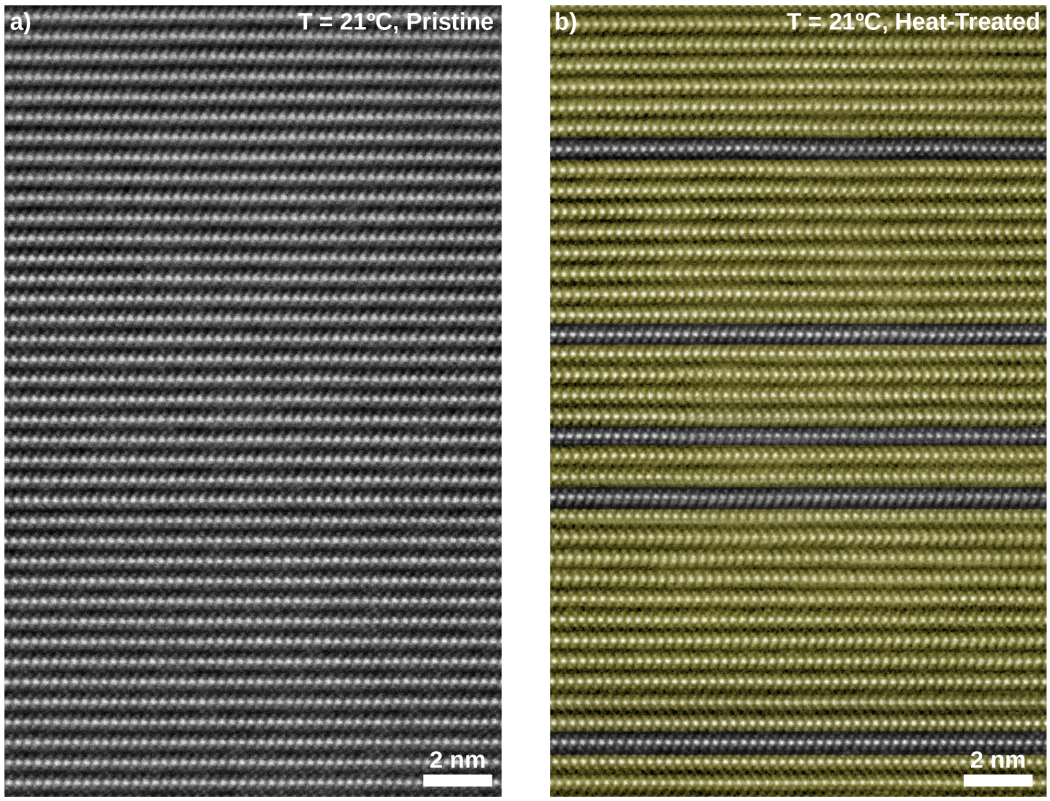

SFIG. S3. **Polytypic transition revealed by cross-sectional HAADF-STEM.** $[10\bar{1}0]$ cross-sectional HAADF-STEM of TaS_xSe_{2-x} of a) pristine, 1T and b) heat-treated polytypic heterostructure. Pr-layers are marked yellow. a) Every layer of 1T-TaS_xSe_{2-x} is initially octahedrally coordinated as expected. b) Heat-treated sample shows Oc→Pr conversion in some of layers. Monolayers of Oc-TaS_2 are shielded in between slabs of Pr-layers. A selenium doped sample was imaged to enhance chalcogen visibility and determine coordination.

Appendix SI5: Cross-sectional SAED

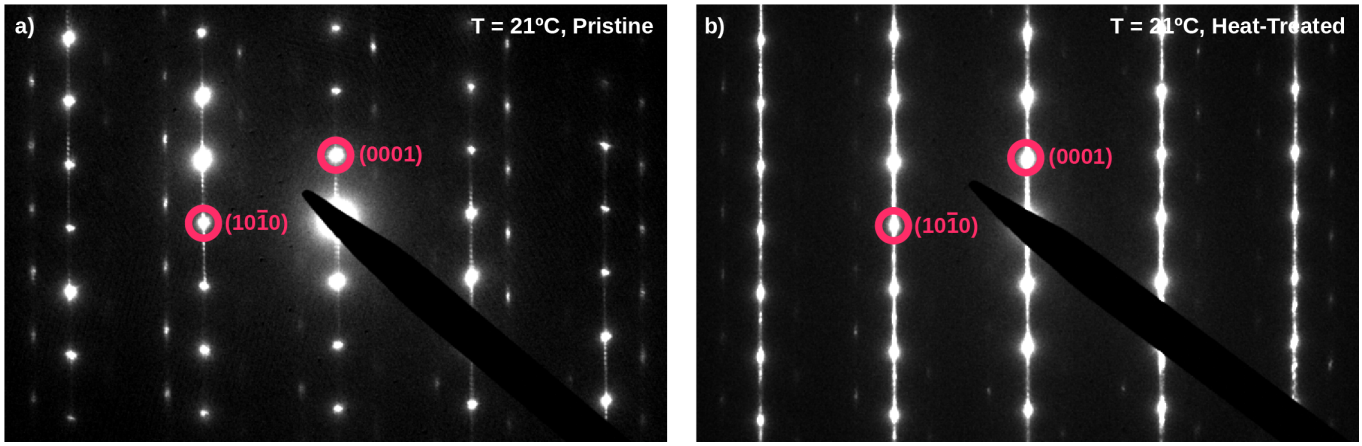

SFIG. S4. **Cross-sectional SAED.** Cross-sectional SAED pattern of a) pristine TaS_2 and b) heat-treated polytypic heterostructure. The heterostructure diffraction shows streakings connecting Bragg peaks along [0001], due to disordered polytypic stacking. This is evidently distinct from 4Hb-TaS_2—ordered mixed polytype phase with alternating Pr–Oc stacking.

Appendix SI6: Phenomenological Landau Model for twin degenerate C-CDW

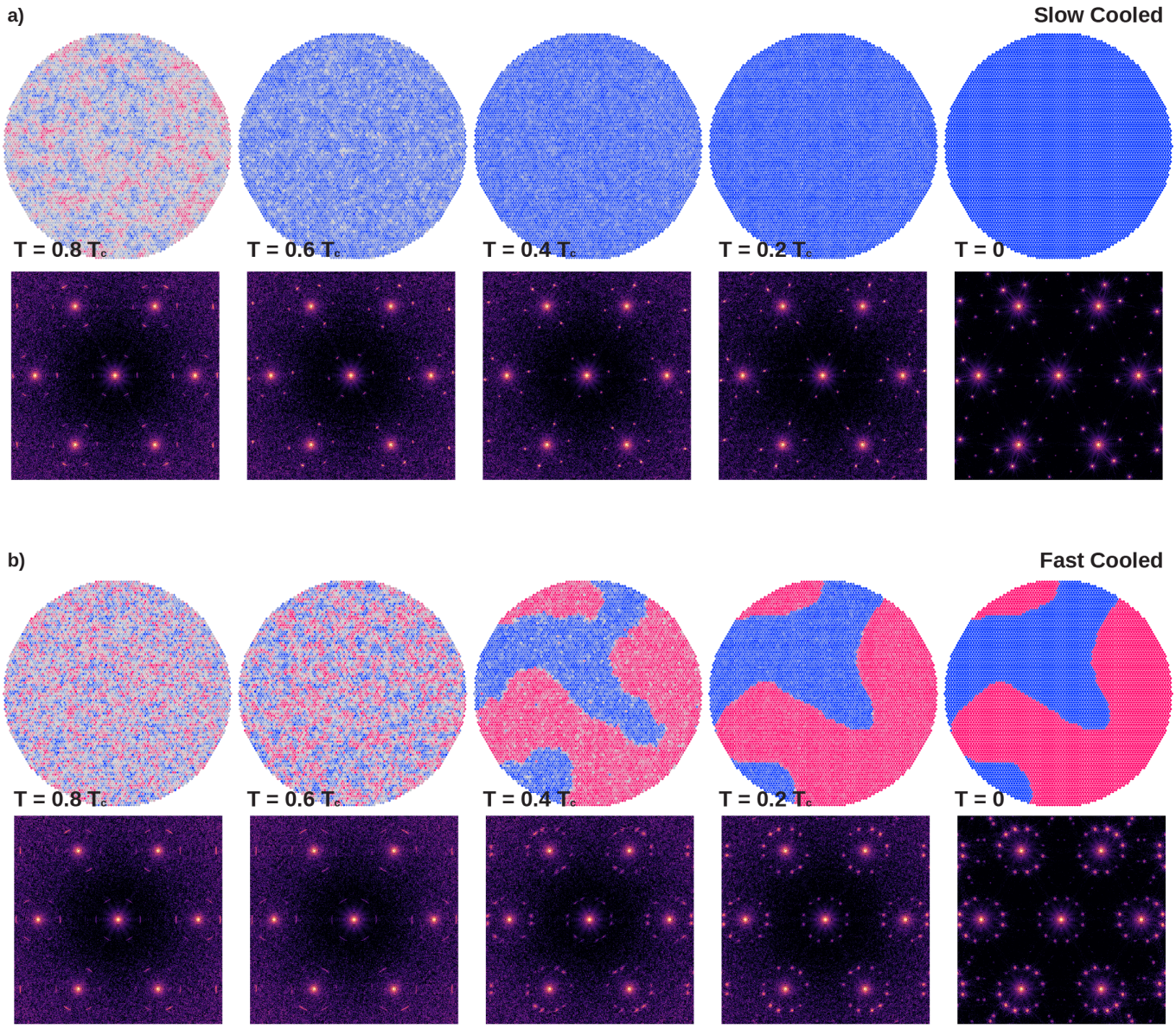

SFIG. S5. **Effect of Cooling Rate for Landau CDW.** a) $A_2 = 1, A_4 = 10, \gamma = 0.5, 10^{10}$ iterations. b) $A_2 = 1, A_4 = 10, \gamma = 0.1, 10^8$ iterations. In slow cooled simulation (a), all lattice sites converged in to single twin, where as fast cooled simulation (b) shows premature cooling allows for in-plane twin.

Appendix SI7: NC/C twin CDW

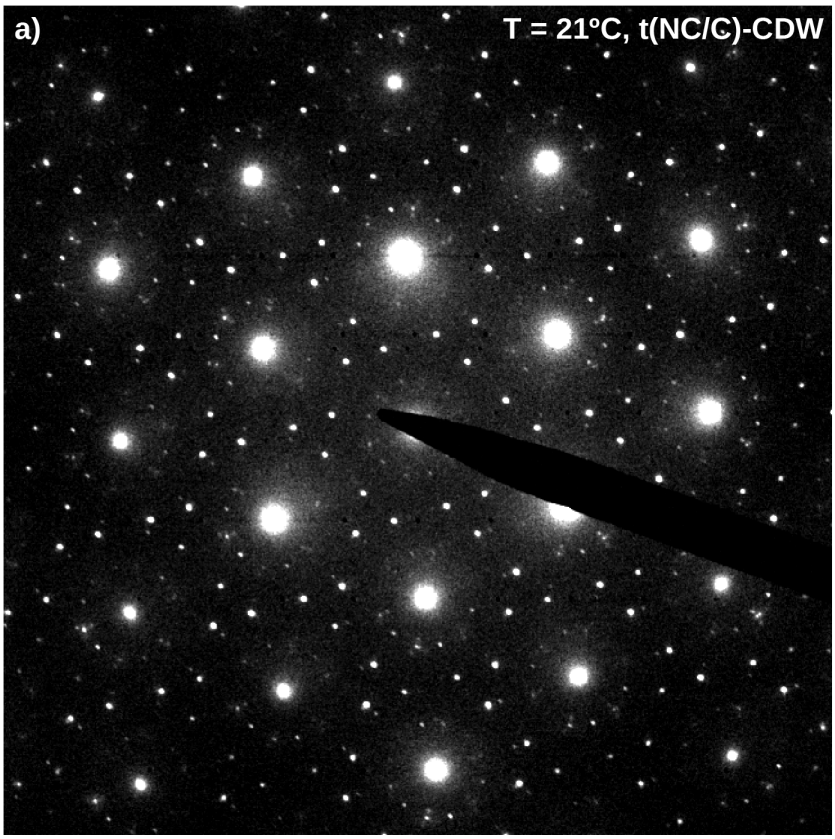

SFIG. S6. **NC-C CDW phase in heat-treated TaS_2.** Insufficient polytypic transition results NC-C twin CDW. The sample likely included both ultra-thin and thick Oc-layers encapsulated between Pr-layers, causing the former to be in commensurate and the latter to be in nearly-commensurate state. Pr-layers decoupled the C and NC layers allowing for co-existence of two states in projection.